JOURNAL OF MATERIALS SCIENCE 17 (1982) 3641–3652

Comparison of the quench rates attained in gas-atomized powders and melt-spun ribbons of Co- and Ni-base superalloys: influence on resulting microstructures

FRANCIS DUFLOS, JEAN-FRANÇOIS STOHR
Office National d'Etudes et de Recherches Aerospatiales, BP No. 72 92322 Chantillon Cedex, France

The cooling rates of gas-atomized Stellite 6 powders range from 10^3 to 10^6 K sec^{-1} for 400 to 10 μm diameter powder particles, respectively. The microstructures vary from the equiaxed type in the coarser particles to dendritic and finally microcrystalline in the finer particles. In the melt-spun ribbons, the microstructure along a cross-section of the ribbon changes from microcrystalline at cooling rates higher than 10^7 K sec^{-1} to columnar dendritic at cooling rates of the order of 10^6 K sec^{-1}.

1. Introduction

With the advent of rapid solidification technologies, ultra-rapid quenching of superalloys has become a subject of considerable interest in the development of aircraft structures and engines. In this respect, the department of Materials Science of ONERA recently launched a research programme on rapid quenching of superalloys. The first objective is to assess the possible benefit that can arise from rapid quenching of nickel-base superalloys and its possible application to discs and turbine blades.

This paper presents the results of preliminary work carried out in the Powder Metallurgy Section at ONERA. The purpose of this work is to establish a quantitative comparison of the quench rates and solidification microstructures obtained with conventional gas-atomized powders on the one hand, and melt-spun ribbons on the other. The paper concentrates mainly on a systematic study of solidification microstructures together with an attempt to correlate cooling conditions and structures.

2. Experimental details

Microstructures of gas-atomized powders were investigated in the cobalt-base superalloy Stellite 6*. This alloy presents a good stability of the dendritic structure over a wide range of cooling rates, thus allowing a precise relationship between secondary dendrite arm spacing (SDAS) and the freezing rate. The Stellite 6 powders studied in the present work were produced by conventional gas atomization with nitrogen as the atomizing gas. The powder heat was then screened to standard size classes ranging from below 40 to 125–400 μm diameter. These size classes were used to characterize the powder and study the microstructure. The use of narrow size classes was especially important in establishing the relationship between the scale of the as-quenched microstructure and the particle diameter since the true particle diameter may not always be observed on a polished surface.

Both nickel- and cobalt-base alloys were spun to ribbon by conventional melt-spinning with a copper roller as the rotating chill substrate. The melt-spinning was done in a purpose-built chamber under an inert atmosphere of pure argon or helium.

The ribbon width was typically 4 mm and the thickness ranged from 27 to 40 μm depending largely on the fluid flow conditions. The morphology of solidification microstructures was observed both by scanning electron microscopy

*Stellite 6 (wt%): Cr 27.7, Sr 1.42, W 4, C 1.22, Bal. Co.

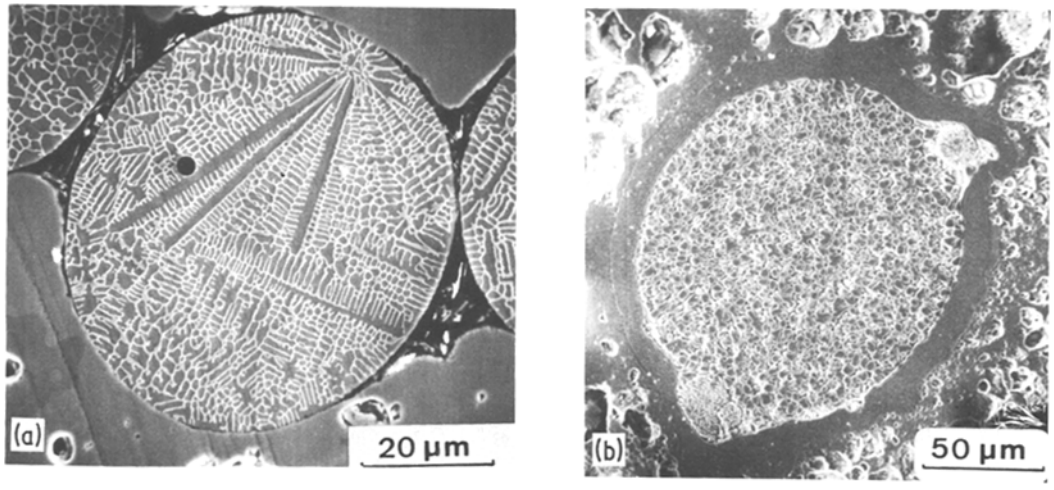

Figure 1 Two types of solidification structures observed in S6 powders. Scanning electron micrographs. (a) Dendritic structure; (b) equiaxed type structure.

(SEM) and transmission electron microscopy (TEM) on etched sections and thin foils, respectively. The melt-spun ribbons were readily suitable for both examinations whereas the loose powders had to be embedded in a nickel matrix by electroplating, to provide suitable conductive specimens for electropolishing. The thin foils were obtained by the conventional "window" thinning technique from the composite nickel-powder foils.

2.1. Solidification microstructures and quench rates in gas-atomized powders and melt-spun ribbons

2.1.1. Gas-atomized stellite 6 powders

2.1.1.1. As-quenched microstructures. Examination of polished and etched sections of embedded Stellite 6 powders by SEM showed that essentially two distinct types of solidification microstructures were present in classical gas-atomized powders. The finer particles, i.e. particles less than 50 μm diameter, exhibited a typical dendritic pattern (Fig. 1a), whereas the coarse fraction of the atomization product (above 100 μm diameter) presented an equiaxed type microstructure (Fig. 1b). The equiaxed microstructure was characterized by the absence of directional growth in a polished section. A statistical study of the solidification microstructures was carried out on a large number of particles ($\sim$ 150) for each powder size class. The results are shown in Fig. 2 where the variation in the fraction of fully dendritic powders is plotted as a function of powder size. The dendritic fraction varies from 6% for the 350 μm diameter particles to 85% for the 20 to 40 μm particles.

It should be noticed that hybrid structures with a few well-developed dendrites within an equi-axed matrix were sometimes observed. These

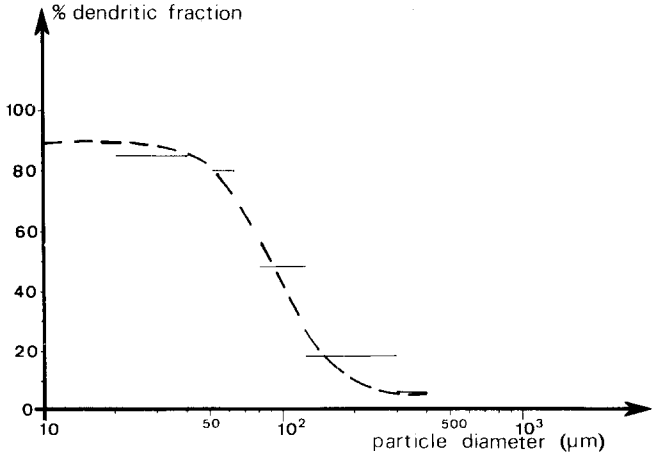

Figure 2 Variation of the fraction of dendritic particles as a function of particle size.

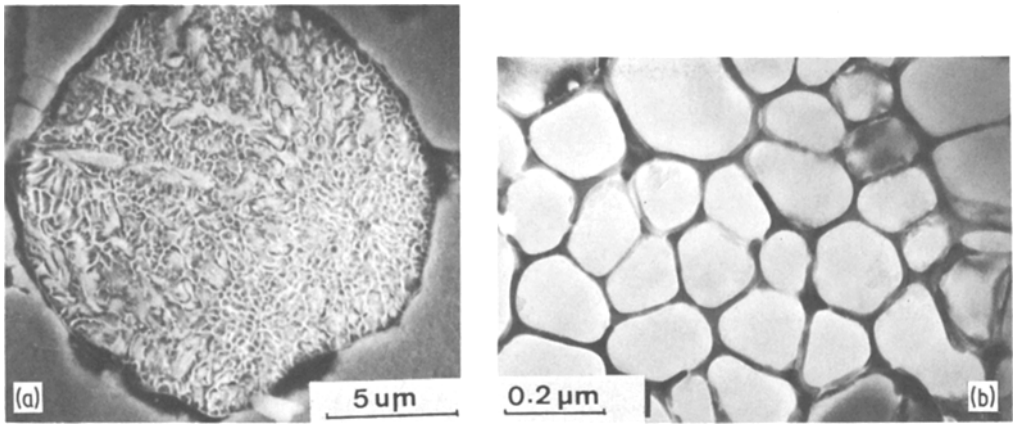

Figure 3 Cellular structure observed in a 15 μm diameter particle. (a) Scanning electron micrograph on a polished section; (b) Transmission electron micrograph on a thin foil.

structures were considered to belong to the dendritic fraction.

In addition, a substantial fraction of the powders, less than 20 μm diameter, exhibited a completely different type of structure which appeared to be cellular or microcrystalline, depending largely on quenching conditions. As shown in Fig. 3, a cellular microstructure was characterized by fairly regular cell walls decorated by a continuous second-phase precipitation. The individual cells, whose dimensions were typically of the order of 0.1 to 0.2 μm, were readily identified by TEM diffraction technique. Ultrafine cellular powder particles (5 to 10 μm diameter) were composed of a very small number of individual cells.

The microcrystalline structure is illustrated in Fig. 4. Combined SEM and TEM study revealed that this structure did not generally extend across the entire ultrafine powder particle. The grain sizes ranged from 0.1 to 0.5 μm. A microcrystalline pattern could be differentiated from a cellular macrocrystalline pattern in two ways: firstly, by selected-area diffraction technique in TEM, and secondly, by the absence of second-phase particles in the grain-boundaries. In general, microcrystalline structures presented increased homogeneity with respect to cellular structures. As illustrated in Fig. 4a, regions adjacent to a cellular or microcrystalline area were frequently dendritic, as expected in the case of fine particles. These observations are qualitatively similar to those reported by Field and Fraser [1] for IN 100 and MM 200 powders.

The second important observation made in Stellite 6 powders concerns the evolution of the scale of the as-quenched microstructure with powder size. Owing to the existence of dendritic powders over the whole powder size range, the

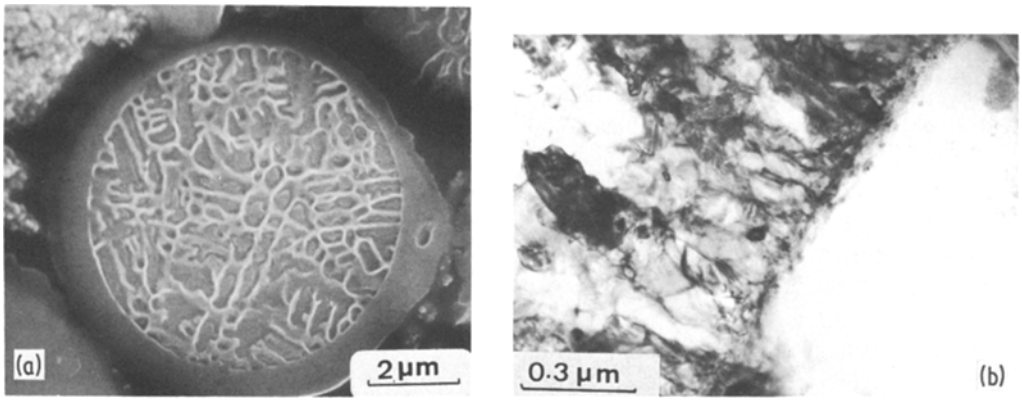

Figure 4 Microcrystalline and cellular structure observed in fine particles 5 to 10 μm diameter. (a) Scanning electron micrograph showing the cellular structure of the core and the featureless structure of the outer shell. (b) Transmission electron micrograph showing the microcrystalline structure of the outer shell.

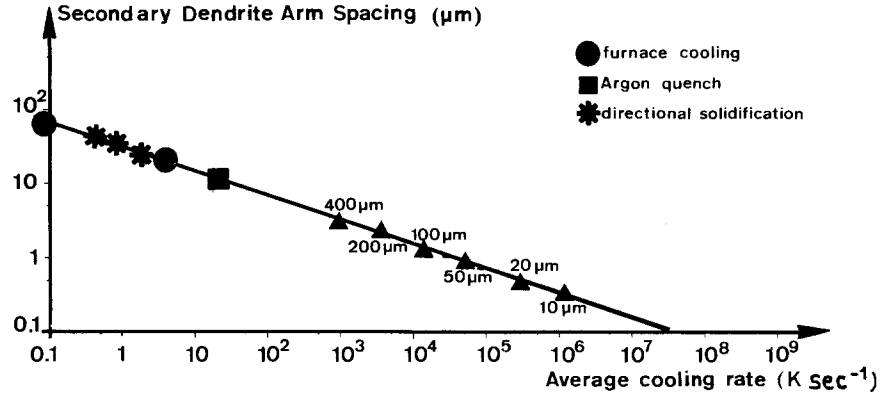

Figure 5 Plot of the secondary dendrite arm spacing (SDAS) for particles of different diameters against cooling rate, and calibration plot.

parameter used to describe the scale of the microstructure was the secondary dendrite arm spacing, d (SDAS).

However, it was rather difficult to obtained SDAS values for ultrafine particles (less than 5 μm) owing to the small amount of fully dendritic powder in this size class. As expected, the variation of SDAS with powder size could be described by a relationship of the type: $d = AD^n$ where D is the particle diameter, A a constant and $n = 0.64$ in the case of Stellite 6 powders. The secondary dendrite arm spacing was found to range (within 10% of the average values) from 3.5 to 0.3 μm for particle diameters ranging from 400 to 10 μm, respectively.

2.1.1.2 Estimation of quench rates in Stellite 6 powders. It is well established that the SDAS, d, can be related to the average cooling rate during solidification, $\dot{T}$, through a simple power relationship of the form [2]

$$d = B\dot{T}^m, \quad (1)$$

where B is a constant. It was therefore decided to establish a calibration plot of $\log d$ against $\log \dot{T}$ over a range of reliably measured cooling rates which could be extrapolated to higher quench rates and thus provide a reasonable estimate of the cooling rates achieved in conventional gas atomization. Specimens of Stellite 6 were quenched at rates ranging from 0.1 to 20 K sec^{-1} using controlled furnace cooling, directional solidification and gas-quench techniques. The results of SDAS measurements and corresponding cooling rates are plotted in Fig. 5 together with the linear extrapolation to quench rates up to 10^7 K sec^{-1}.

SDAS values obtained in powders could then be plotted in Fig. 5 and the corresponding cooling rates for various particle size classes evaluated. The quench rates in Stellite 6 powders ranged from 9×10^2 K sec^{-1} for 400 μm diameter particles to 2.8×10^5 K sec^{-1} for 20 μm diameter particles.

On the basis of the above considerations, one may tentatively suggest that rapidly quenched powders could be conveniently obtained through a simple screening to less than 20 μm diameter powders. However, this would not be a technologically realistic approach since this fraction represents only 5% of a conventional gas-atomization product.

According to the above power relationship (Equation 1), 5 to 10 μm diameter particles were quenched at rates exceeding 10^6 K sec^{-1}. It is not clear at this stage whether the $\dot{T}$ powder size relationship can still be reasonably applied to powder size classes where fully dendritic structures were not frequently observed.

2.1.2. Melt-spun ribbons of Co and Ni-base superalloys

2.1.2.1. As-cast microstructures. The cobalt-base alloy Stellite 6 and a nickel-base alloy C 146* with a high aluminium content were spun to ribbons under an argon atmosphere using a copper roller. Both alloys exhibited the same basic grain structure as revealed by SEM examination, similar to that reported by Davies *et al.* [3] in Nimonic alloys.

*C 146 (wt %): Co 5, Cr 4, Mo 2, W 6, Ta 6, Ti 1, Hf 1.5, Al 7.5, C 0.1, Bal. Ni.

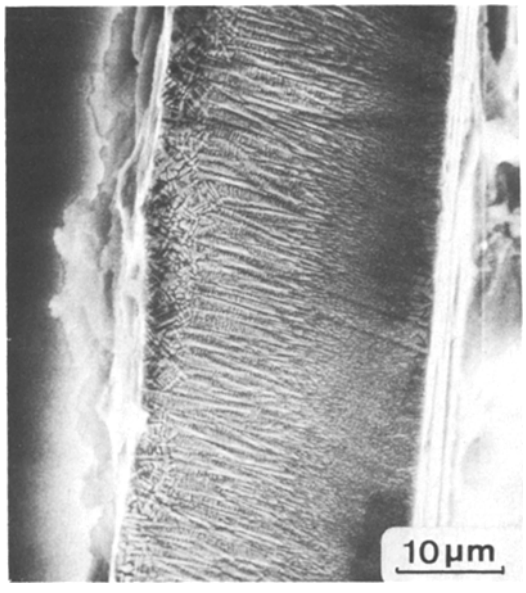

Figure 6 Typical solidification structure of a S6 melt-spun ribbon. Scanning electron micrograph on a polished section.

(a) Stellite 6 alloy. The typical solidification microstructure observed in a 30 μm thick S6 ribbon (Fig. 6) clearly exhibited three distinct zones:

(i) a fairly featureless chill zone, about 4 to 5 μm thick;

(ii) a columnar dendritic region usually extending across the major part of the ribbon thickness (20 μm);

(iii) a randomly oriented dendritic region 3 to 4 μm thick extending to the top surface of the ribbon. There was no appreciable change in the SDAS across the ribbon thickness; in fact, SEM resolution was sufficient to show that in Stellite 6 ribbons the SDAS ranged from 0.17 to 0.26 μm for the columnar dendritic and the randomly oriented dendritic zone, respectively.

The gradation of structure through the ribbon thickness was investigated in more detail by polishing at different levels within the ribbon thickness. Thin foils in the bottom section of the ribbon, close to the chill block, were readily obtained by electropolishing from one side. The change in microstructure from the chill surface to the top surface region of Stellite 6 ribbons is shown in Fig. 7. Transmission electron micrographs (Fig. 7a) clearly showed the microcrystalline structure of the region close to the chill block, with a grain size ranging from 0.2 to 0.5 μm. At a somewhat higher level of observation through the thickness, the grains were found to be subdivided into a cell structure (Fig. 7b) whose walls consisted of a second phase. In this transition zone, the cells had an equi-axed section although their morphology was probably columnar. The cell diameter, which varied slightly from the chill zone across the cellular region, was typically of the order of 0.2 μm. Examination of the columnar dendritic region revealed no carbide precipitation within the dendrite cores (Fig. 7c). Close to the top surface, the randomly oriented dendrites (Fig. 7d) exhibited a SDAS of 0.26 μm consistent with the SEM examinations.

(b) C 146 alloy. Similar observations were made in a 43 μm thick C146 ribbon where SDAS values were typically about 0.36 μm (Fig. 8a). However, it should be emphasized that the randomly oriented dendritic zone was not necessarily present in the solidification structure of this alloy, especially in ribbons where the homogeneous chill zone extended across almost half the ribbon thickness. Very few details were sometimes resolved within the chill zone where the average grain size appeared to be smaller than 1 μm (Fig. 8b). Fig. 9 shows a set of transmission electron micrographs in a 40 μm thick C146 ribbon obtained at different levels of observation within the ribbon thickness. The gradation of structure from the chill zone to the top surface was strictly comparable to that observed in S6 ribbons described above. However, in this nickel-base alloy, two types of precipitates were observed, namely MC type carbides and the ordered γ'-phase. The γ'-phase was present across the entire ribbon thickness with γ' precipitate size ranging from 10 to 30 nm. The carbide particles were somewhat different in the microcrystalline region as compared to the columnar dendritic zone. In the microcrystalline region with a grain size ranging from 0.3 to 1 μm, carbide precipitation occurred both at the grain boundaries and within the grains. Within the grains, the carbide precipitation was very homogeneous with a very small particle size ranging from 3 to 10 nm (Fig. 9b). The presence of a precipitate-free zone in the vicinity of the grain boundaries indicated very high quench rates in the chill zone. In the cellular zone (Fig. 9c) the grains, about 1 μm diameter, were subdivided into 0.1 μm diameter cells. In this zone, the carbides appeared to have precipitated within the cell walls exclusively. As shown in

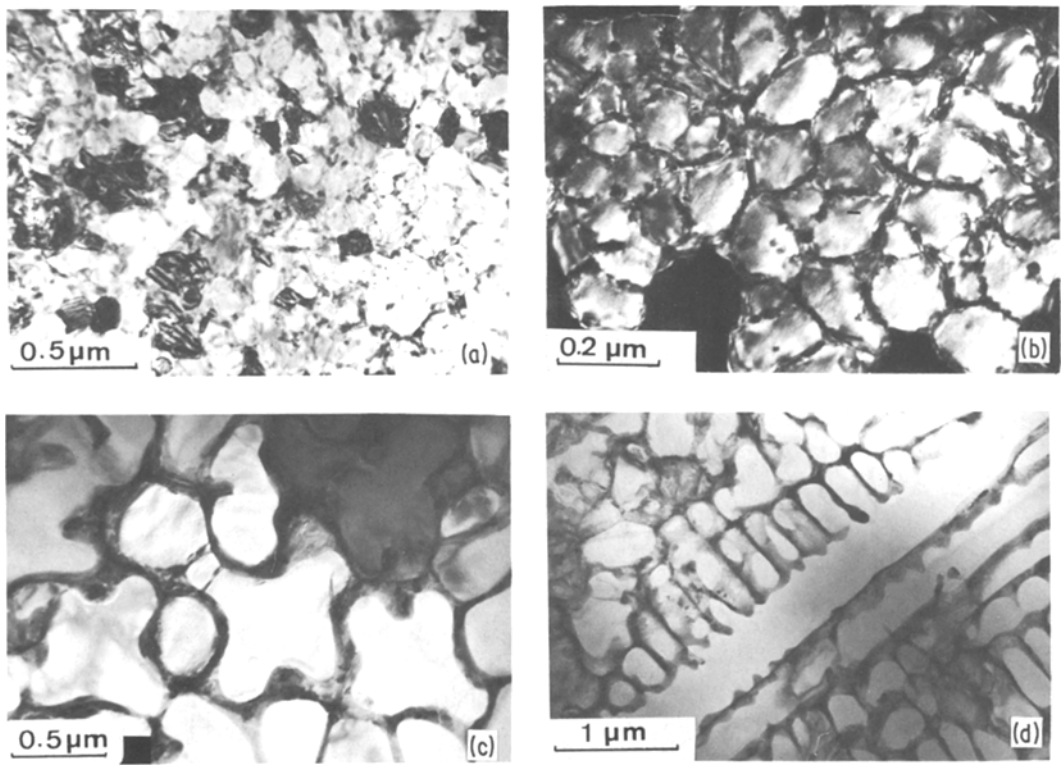

Figure 7 Different types of microstructures observed by transmission electron microscopy in a Stellite 6 ribbon section. (a) Microcrystalline structure; (b) cellular structure; (c) columnar dendritic structure; (d) randomly oriented dendritic structure.

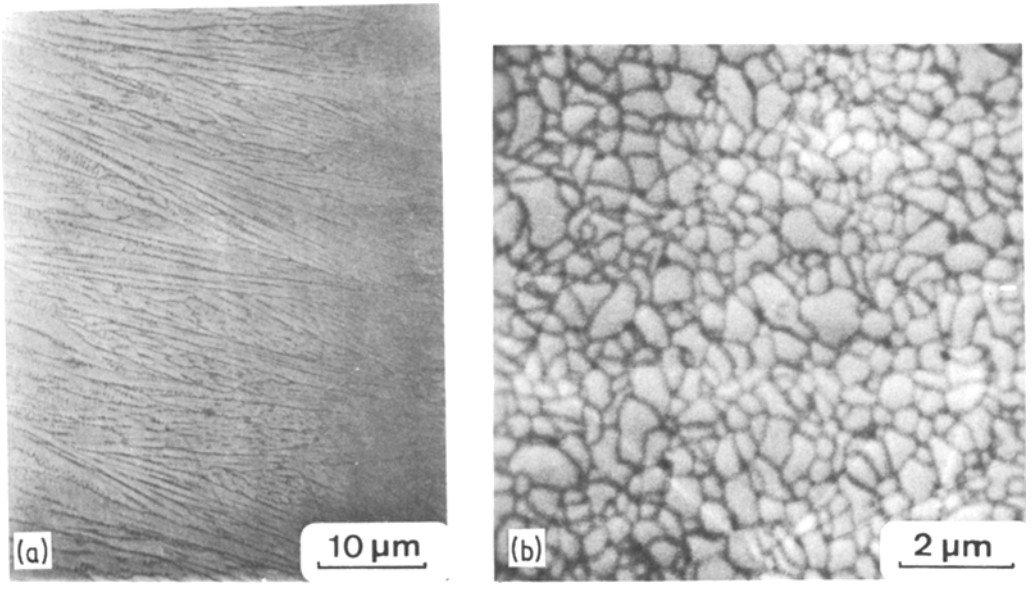

Figure 8 Solidification microstructure of a C 146 melt-spun ribbon (scanning electron micrographs). (a) Section of the ribbon; (b) Polished and etched chill-zone.

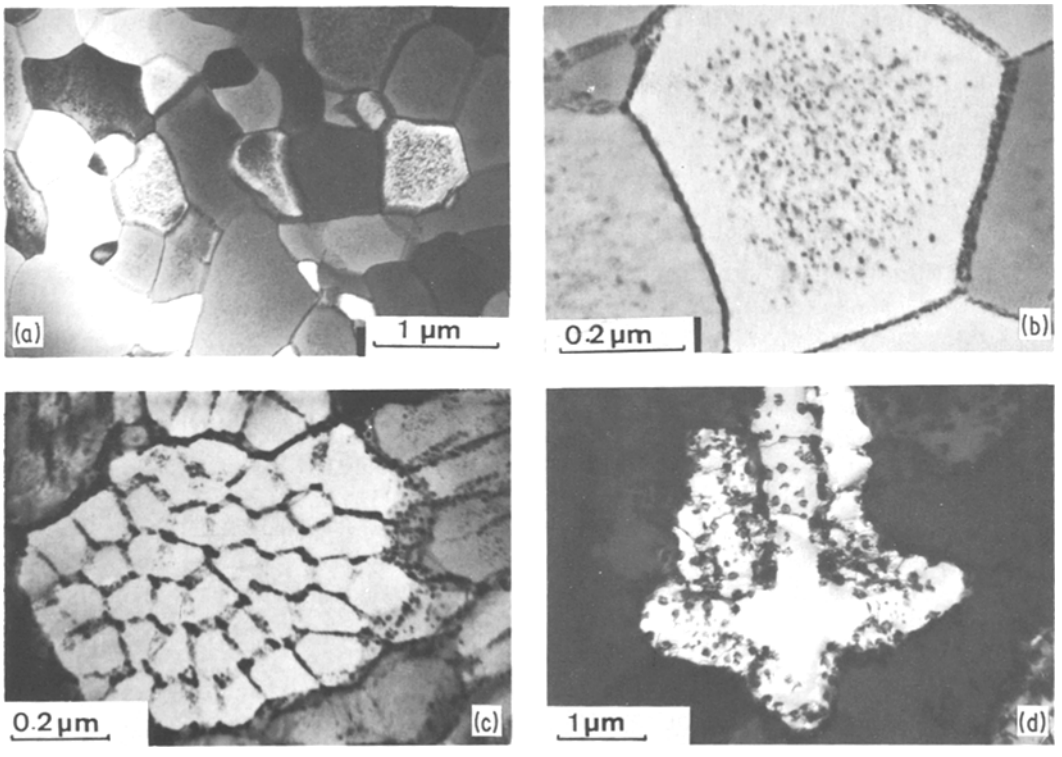

Figure 9 Different types of microstructure observed by transmission electron microscopy in a C 146 melt-spun ribbon. (a) and (b) Microcrystalline structure; (c) cellular structure; (d) columnar dendritic structure.

Fig. 9d, the change from columnar–cellular to columnar–dendritic was very drastic. The entire columnar dendritic region was characterized by a relatively fine dispersion of MC type carbide having a somewhat higher diameter which ranged from 30 to 100 nm, as opposed to the microcrystalline region.

2.1.2.2. Estimation of quench rates. As in the case of powder particles, SDAS measurements were used to estimate the quench rates achieved in melt-spun ribbons during solidification. For each alloy, a calibration plot was established (see description in Section 2.1.1.) which was extrapolated to small SDAS values to allow estimation of the quench rate.

The cooling rate in Stellite 6 ribbon was found to lie between 2×10^6 and 6×10^6 K sec^{-1}, corresponding to SDAS values of 0.26 and 0.17 μm, respectively. Owing to the inherent error encountered with such a linear extrapolation, the cooling rate during solidification averaged over the ribbon thickness can be safely estimated to be 5×10^6 K sec^{-1}.

Similar considerations led to a value of 3×10^6 K sec^{-1} in a 43 μm thick C 146 ribbon (for SDAS values of 0.36 μm). These two estimations should be regarded as being representative of the columnar dendritic zone since the chill zone was devoid of any dendritic solidification. In the latter region, a simple calculation based upon the diffusion of carbon in nickel, together with the measurement of the width of the precipitate-free zone close to the grain boundaries was used to estimate the quench rate during solidification. Let C_o be the carbon concentration in the alloy. Assuming that no carbide precipitation occurs when $C = C_o/10$, the width, d, of the precipitate-free zone will be determined by $d^2/4Dt = 2.3$ where D is the diffusion coefficient of carbon in nickel [4], and t the time. Fig. 9b shows that the width, d, of the precipitate-free zone in C146 was $\sim d/2 = 3.85 \times 10^{-5}$ cm. This leads to a value of 7×10^7 K sec^{-1} for the quench rate. The choice of $C_o/10$ as a critical concentration value is arbitrary and has no strong influence on the estimated value of the quench rate.

It can therefore be concluded that the cooling rate achieved in the immediate vicinity of the chill substrate was higher than 5×10^7 K sec^{-1} in C146

alloy. Similar high quench rates are certainly achieved for the chill zone in the case of Stellite 6 ribbons. It should be borne in mind that only a few micrometers close to the wheel experienced such high freezing rates.

2.2. Interpretation of solidification microstructures in powders based on the thermal history of droplets

2.2.1. Heat transfer calculations for convectively cooled droplets

In order to obtain a better understanding of the heat flow and solidification behaviour of convectively cooled droplets, cooling conditions were studied using the solidification time, t_s, as the determining parameter. For this purpose, t_s was evaluated in two ways.

Firstly, a simple estimation of t_s was made from the measured quench rates, $\dot{T}$, using the relationship $t_s = \Delta T/\dot{T}$, where ΔT is the freezing range of the alloy [2]. In this case, t_s was assimilated to the local solidification time considering that only a few dendrites were usually present within a single particle. The values of "measured" solidification times, together with corresponding particles diameters, are listed in Table I.

Secondly, t_s was calculated in two different ways, using either a simple relationship valid in the case of a Newtonian cooling regime or a computed heat transfer simulation. The assumption of Newtonian cooling is supported by the fact that, in the case of convectively cooled droplets ranging from 50 to 400 μm, the Biot number remains below 0.1 [5]. Under these conditions, the solidification time can be simply derived as follows:

$$t_s = (R\rho H\Delta T)/[3h(T - T_o)] \qquad (2)$$

where R is the radius of the droplet, T_o the temperature of the atomizing gas, H the heat of fusion, ρ the density of the alloy, and h the heat transfer coefficient. In the case of the simulation, the model used to compute the solidification time, similar to that proposed by Glickstein *et al.* [6] assumes that the solidification begins at the surface of the droplet and that the solid–liquid interface moves into the droplet as a spherical shell. In this model, the droplet is not isothermal. Both calculations gave similar values of the solidification time for values of h up to 2×10^4 W m^{-2} K^{-1}. For values of h ranging from 2×10^4 to 1.2×10^5 W m^{-2} K^{-1}, discrepancies between the values of t_s were typically less than 10%.

TABLE I Solidification time, t_s, in Stellite powders, estimated from $t_s = \Delta T/\dot{T}$

Particle diameter (μm)	Cooling rate $\dot{T}$ (K sec^{-1})	t_s (μsec)
400	9×10^2	7.78×10^4
200	3.4×10^3	2.06×10^4
100	1.4×10^4	5×10^3
50	5×10^4	1400
20	2.8×10^5	250
10	1.1×10^6	63.6
5	2.5×10^6	28

Calculation of the solidification time for each particle size class requires the knowledge of the combined radiative and convective heat transfer coefficient. The radiative contribution was found to remain negligible as compared to the convective term within the size range considered. The contribution of radiative cooling ranged from 10% in the case of 200 μm diameter particles to 0.6% for 10 μm diameter particles. The convective heat transfer coefficient was estimated from the following equation:

$$hRk_g = (1 + 0.3(Re)^{1/2})\mathscr{P}r^{1/3} \qquad (3)$$

k_g is the thermal conductivity of the atomizing gas, R the particle radius, (Re) the Reynolds number and $\mathscr{P}r$ the Prandtl number

$$(Re) = 2VR\rho_g/\mu_g \qquad (4)$$

$$\mathscr{P}r = C_g\mu_g/k_g, \qquad (5)$$

where V is the relative gas-particle velocity, ρ_g, μ_g, C_g the density, viscosity and specific heat of the gas, respectively. Equation 4 points out that evaluation of the heat transfer coefficient requires a precise knowledge of the relative gas-particle velocity for each particle diameter. Owing to the difficulty of measuring this latter parameter with sufficient accuracy, it was decided to calculate the values of the relative gas-particle velocity that would permit agreement between the calculated values of the solidification time and those obtained from the experimental values of the quench rates. Results are shown in Table II. Under these conditions, particles larger than 100 μm diameter were found to have relative velocities of the order of 100 m sec^{-1}, which is in good agreement with values obtained through fluid dynamic equations. On the other hand, for particles smaller than 100 μm, the calculations yielded relative velocities larger than the atomizing gas velocity, indicating an unrealistic approach to the phenomena, i.e.

TABLE II Relative gas-particle velocities as determined by equating h (measured) and h (calculated)

Particle diameter (μm)	h (measured) = h (calculated) (W m^{-2} K^{-1})	V (msec^{-1})
400	1.76×10^3	52
200	3.39×10^3	123
100	7.52×10^3	354
50	1.25×10^4	497
20	2.84×10^4	1038
10	5.43×10^4	1904

convective and radiative cooling alone cannot explain the high solidification rates achieved in the finer particles.

In order to obtain some insight into the different phenomena which can explain the high quench-rates observed for the finer particles, the maximum convective cooling that can be achieved during the atomization has been evaluated as follows:

(i) for particles larger than 100 μm it is possible to match the experimental and the calculated values of the solidification time using realistic values of the relative gas-particle velocity;

(ii) for particles smaller than 100 μm, the relative gas particle velocity was taken equal to its maximum possible value, i.e. the atomizing gas velocity. Values of the solidification time hence calculated are listed in Table III together with the values of the solidification time deduced from experimental data. It should be noted that for particles smaller than 100 μm, the "measured" values of the solidification time are much smaller than the calculated values. As stated before, this discrepancy clearly demonstrates that the high quench rates achieved in the finer particles cannot be explained by combined convective and radiative cooling only, since the combined radiative and convective cooling has been taken as its maximum possible value. The sole phenomenon which can account for experimental solidification times smaller than the calculated ones must be undercooling of the melt. This can be explained as follows.

As shown by Equation 2, the solidification time is directly proportional to the latent heat of fusion H. Therefore, the amount of heat to remove by convective cooling will be smaller in an undercooled droplet. Let a droplet be undercooled from the melting point, T_m, to the nucleation temperature, T_1, the heat to remove by convective cooling to complete solidification is $H - C_p(T_m - T_1)$, where C_p is the mean specific heat of the solid and the liquid. The solidification time of an undercooled droplet is therefore reduced by a factor

$$R = 1 - \frac{C_p}{H}(T_m - T_1). \quad (6)$$

The degree of undercooling in Stellite 6 atomized powders was calculated in the present work by adjusting the computed and the measured values of the solidification time, using Equation 5 (Table III).

In summary, results of the heat flow calculation carried out to study solidification conditions in a conventional nitrogen atomization showed that:

(a) convective cooling alone is sufficient to achieve quench rates ranging from 10^3 to 10^4 K sec^{-1} in powder particles of 400 to 100 μm diameter, respectively.

(b) high quench rates experienced by the smaller particles result essentially from a high undercooling, typically 200 K for 10 μm diameter particles.

2.2.2. Interpretation of solidification microstructures in nitrogen atomized Stellite 6 powders

2.2.2.1. Equi-axed structure. As described in Section 1.1, the major fraction of the large particles exhibit a coarse-grained equiaxed structure, with only a small fraction having a dendritic structure. The equiaxed structure can be interpreted as

TABLE III Calculated t_s and corresponding degree of undercooling when accounting for the real gas-particle velocity during atomization

Particle diameter (μm)	h (measured) (W m^{-2} K^{-1})	h (calculated) (W m^{-2} K^{-1})	t_s (measured) (μsec)	t_s (calculated) (μsec)	Undercooling (K)
400	1.76×10^3	1.76×10^3	7.78×10^4	7.78×10^4	0
200	3.39×10^3	3.39×10^3	2.06×10^4	2.06×10^4	0
100	7.52×10^3	7.48×10^3	5×10^3	5×10^3	0
50	1.25×10^4	1.07×10^4	1400	1600	53
20	2.84×10^4	1.76×10^4	250	400	158
10	5.43×10^4	2.62×10^4	63.6	130	207

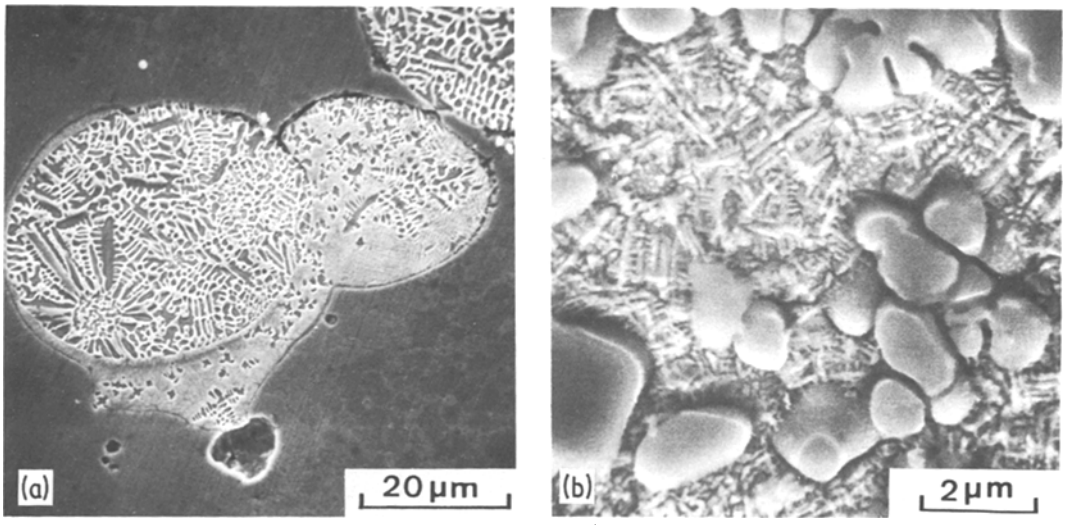

Figure 10 Splat showing the intermediate solidification stage (scanning electron micrograph). (a) Low magnification; (b) high magnification micrograph showing the fine dendritic structure.

the consequence of nucleation on fragments of predendrites. These fragments of predendrites may result from partial dissolution of predendrites in a way similar to that produced by a processing technique known as stir-casting in which semi-solid material containing predendrites is highly sheared during cooling through the melting-range. Such a mechanism is strongly suggested in Fig. 10a; the splatted material was produced by collision between a semi-solid mushy particle and a solid substrate particle. Fragments of dendrites are clearly visible, and illustrate the intermediate solidification stage suggested above. The remaining liquid was very efficiently quenched by conduction heat transfer towards the chilled particle, thereby developing a very fine dendritic structure as shown in Fig. 10b.

2.2.2.2. Dendritic structure. In the finer fraction of the atomization product, typically less than 100 μm diameter, a large fraction of the particles present a fine dendritic structure, with very few dendrites per particle. This structure results from heterogeneous nucleation occurring in highly undercooled droplets. Heterogeneous nucleation is likely to take place during the solidification flight of fine particles owing to numerous collisions experienced by the fine particles. Growth of a dendrite across the entire particle is thereby rendered possible due to the high degree of undercooling existing in such fine particles.

2.2.2.3. Massive transformation. In the ultrafine size range, i.e. particles less than 10 μm diameter, three types of solidification microstructures are found, namely, dendritic, cellular, and microcrystalline.

The cellular structure, which has been described in Section 2.1.1, usually developed across most of the particle section. It is interesting to note the occurrence of a microcrystalline structure with no segregation at the grain boundaries (Fig. 4b). High-magnification scanning electron micrographs revealed no discernable features within the microcrystalline zone (Fig. 4a). Microcrystalline zones were frequently confined to the periphery of ultrafine particles ($\sim 5\,\mu$m diameter) forming a homogeneous shell about 1 to 2 μm thick. All the evidence to date indicates that this structure formed by a massive transformation resulting from homogeneous nucleation at a high degree of undercooling. It was not possible to detect fully microcrystalline particles in Stellite 6 powders. This seems to indicate that quench rates attained in nitrogen atomized powders, even in the ultrafine size range, were not sufficient to achieve the high degree of undercooling required for complete massive transformation. In fact, the minimum undercooling required to complete solidification without segregation, (i.e. without attaining the solidus temperature), can be easily estimated as suggested by Mehrabian [2]:

$$C_p[(T_L - T_1) + (T_s - T_L)] \geqslant H, \qquad (7)$$

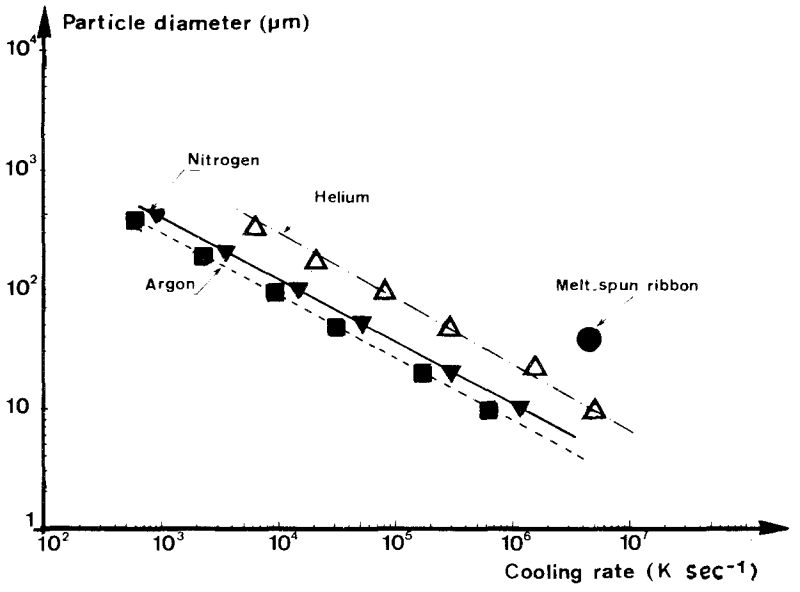

Figure 11 Comparison of quench rates obtained by gas-atomization and melt-spining.

where T_L is the liquidus temperature. According to Equation 7, the undercooling $(T_m - T_1)$ must exceed 490 K in cobalt-base superalloys. Let us consider a typical microcrystalline structure as illustrated in the outer zone of Fig. 4a. The volume fraction that solidified massively represents about 40% of the particle volume. Correlatively, the amount of undercooling estimated from the fraction that solidified massively is 492 K × 0.40 = 197 K. Besides, the solidification time, t_s, that can be estimated from the quench-rate measurements using the relationship $t_s = \Delta T/T$, where ΔT is the melting range of the alloy, is close to 23 μsec for the 5 μm diameter particle considered here. Calculations similar to those described in Section 2.2.1 lead to a value of 41 μsec. Using Equation 6 allowed us to estimate an undercooling of 215 K, in agreement with that determined previously from the fraction of the droplet that solidified massively.

The above considerations clearly establish that the degree of undercooling required to produce fully microcrystalline powders cannot be attained by classical gas atomization. Moreover, the observation of partially microcrystalline powder particles did confirm the calculated amount of undercooling in Stellite 6 powders.

2.3. Comparison of the quench rates attained in gas-atomized powders and in melt-spun ribbons

The objective of the present preliminary work was to assess the range of cooling rates attainable by two distinct techniques, with a view to producing interesting structures and precipitations in superalloys. In this respect, the first objective was to compare cooling rates values as estimated in gas-atomized powders and melt-spun ribbons. For this purpose, quench rates attainable through gas atomization using argon, nitrogen and helium were plotted as a function of particle diameter as shown in Fig. 11. It should be noticed, however, that the rapid solidification processing (RSP) atomization technique illustrated in Fig. 11 is the one developed by Pratt and Whitney Aircraft, using forced convective helium cooling and hence permitting somewhat higher gas velocities than those achieved in gas atomization. Values plotted in Fig. 11 are representative of typical nickel- or cobalt-base superalloys. It is worth mentioning that in a conventional nitrogen-atomization the powder fraction ranging from 150 to 400 μm diameter, which represents 60% of the atomization product, is quenched at rates of the order of $10^3\,K\,sec^{-1}$. The RSP technique developed by Pratt and Whitney produces the same percentage of 60% in the size range 50 to 100 μm [1]. This constitutes a considerable achievement since 60% of the powder heat is therefore manufactured at quenched rates of approximately $10^5\,K\,sec^{-1}$. Equivalent performance in conventional gas-atomization would require screening to the 20 to 40 μm particle size range. This approach is clearly unrealistic since the latter range represents only

6 wt% of the atomization product in the case of nitrogen-atomized Stellite 6, for instance.

A detailed investigation of the microstructures of melt-spun superalloy ribbons revealed that the entire ribbon is cast at quench rates exceeding 10^6 K sec^{-1}. Moreover, the fine homogeneous precipitations of strengthening phases found in melt-spun nickel-base alloys seem to indicate that optimum benefit from rapid quenching processing will be achieved at quench rates higher than 10^6 K sec^{-1}.

Consequently, it was decided to direct future effort towards further studies of melt-spun superalloys. The goal of the forthcoming work is firstly to optimize melt-spinning process parameters for high melting point materials such as nickel- or cobalt-base superalloys, and secondly to adapt superalloy compositions to rapid quenching processing. The objective thereafter is to investigate the thermal stabilities of the products and the properties of consolidated materials.

3. Conclusions

(1) Superalloy powders obtained by classical gas atomization are quenched at rates ranging typically from 5×10^3 to 3×10^4 K sec^{-1}, whereas forced convective cooling using helium yields cooling rates of the order of a few 10^5 K sec^{-1} for about 60% of the powder heat.

(2) In all cases, superalloy powders present a dendritic or cellular solidification microstructure.

(3) Melt-spun ribbons of cobalt- and nickel-base superalloys are quenched at rates faster than 10^6 K sec^{-1}. Examination of melt-spun microstructures clearly demonstrates that to obtain genuine, wholly microcrystalline structures in superalloys requires quench rates in excess of 10^7 K sec^{-1}.

(4) In nickel-base alloys, cooling rates of the order of 10^6 K sec^{-1} are sufficient to produce fine, homogeneous precipitations of strengthening phases such as MC-type carbides.

References

1. R. D. FIELD and H. L. FRASER, 1st Conference on Rapid Solidification Processing, Reston, Virginia, November 1977, edited by R. Mehrabian, B. H. Kear and M. Cohen, (Claitors, Baton Rouge, 1978) p. 270.
2. R. MEHRABIAN, *ibid.* p. 9.
3. H. A. DAVIES, N. S. SHOHOJI and D. H. WARRINGTON, 2nd Conference on Rapid Solidification Processing, Reston, Virginia, March 1980, edited by R. Mehrabian, B. H. Kear and M. Cohen, (Claitors, Baton Rouge, 1980) p. 153.
4. Y. ADDA and J. PHILIBERT, "La Diffusion dans les Solides" (Presses Universitaires de France, Paris, 1966).
5. S. C. HSU, S. CHAKRAVORTY and R. MEHRABIAN, *Met. Trans. B*, 9 (1978).
6. M. R. GLICKSTEIN, R. J. PATTERSON II, N. E. SHOCKLEY, 1st Conference on Rapid Solidification Processing, Reston, Virginia, November 1977, edited by R. Mehrabian, B. H. Kear and M. Cohen (Claitors, Baton Rouge, 1978) p. 46.

Received 14 June
and accepted 21 June 1982